ACS APPLIED NANO MATERIALS

www.acsanm.org

Article

Laser-Patterned Porous Carbon/ZnO Nanostructure Composites for Selective Room-Temperature Sensing of Volatile Organic Compounds

Huize Wang, Pablo Jiménez-Calvo, Marco Hepp, Mark Andrew Isaacs, Charles Otieno Ogolla, Ines Below-Lutz, Benjamin Butz, and Volker Strauss*

Cite This: *ACS Appl. Nano Mater.* 2023, 6, 966–975

Read Online

ACCESS | Metrics & More | Article Recommendations | Supporting Information

ABSTRACT: The development of mobile, noninvasive, and portable sensor technologies for diagnostics and emission control is highly demanded. For that purpose, laser carbonization is studied as a tool to produce responsive carbon materials from inexpensive organic precursors for the room-temperature selective detection of volatile organic compounds (VOCs) applicable in future sensor array-based devices. To increase the response of intrinsically low-responsive laser-patterned carbons (LP-C) to analytes in the gas phase, we tested carbonization in the presence of nanoscale ZnO precursors in primary inks. Following the addition of a zinc salt, $Zn(NO_3)_2$, a noticeable 43-fold increase in the sensor response ($\Delta R/R_0 = -21.5\%$ toward 2.5% acetone) was achieved. This effect is explained by a significant increase in the measurable surface area up to ~700 $m^2 \cdot g^{-1}$ due to the carbothermic reduction supported by the in situ formation of ZnO nanoparticles. Varying Zn concentrations or the addition of as-prepared ZnO nanorods lead to different surface properties like the surface area, porosity, and polarity of LP-C. A predominant effect of the surface polarity on the selectivity toward different analytes of the sensors during physisorption, e.g., acetone vs toluene, was identified and tested. The best-performing LP-C sensors were finely characterized by transmission/scanning electron microscopies and X-ray photoelectron/energy-dispersive X-ray/Raman spectroscopies.

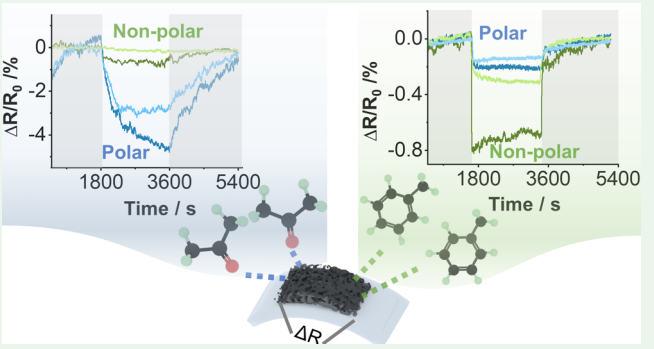

KEYWORDS: *carbon laser patterning, laser carbonization, carbon/zinc oxide nanocomposites, VOC sensing, carbonization, chemiresistor, chemisensor*

INTRODUCTION

Volatile organic compounds (VOCs) are human-made contaminants in indoor environments as well as indicators for diseases.[1] Instruments for precise VOC concentration monitoring are in high demand, first for identification and second for preventing diseases.[2,3] For example, diabetes can be prevented in time by detecting acetone in exhaled breath.[4,5] Among the conventional methods for gastrointestinal disease diagnosis are colonoscopies, tissue biopsies, or antimicrobial swab cultures.[6] All of these techniques present the same drawbacks of being (semi-)invasive, time-consuming, expensive, and not scalable and requiring sophisticated chemical analysis instruments. On the other hand, indoor air quality control (hospitals) is an important analysis, typically conducted by certified large-scale chamber testing facilities (EN 16516). General physical analysis methods that can perform indoor gas detection include gas-chromatography, mass spectrometry, quartz-crystal microbalance, or Fourier transform infrared spectroscopy (FT-IR) spectroscopy, while physicochemical methods include mainly the use of electrochemical cells.[7]

For these reasons, mobile noninvasive chemical detection methods toward VOCs are promising for substituting the conventional complicated methods.[8] With the rapid development of artificial intelligence (AI) and machine learning algorithms, small-scale sensor array technologies have again moved into the focus of attention as a tool for the realization of electronic noses.[9,10] First mobile commercial products based on sophisticated nanotechnology are currently in the final phase of development.[11] Typical materials used for the selective detection of VOCs are metal oxide-based semiconductors,[12] nonviable for long term due to their low

Received: October 4, 2022
Accepted: December 28, 2022
Published: January 17, 2023

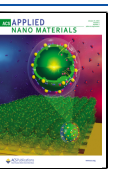

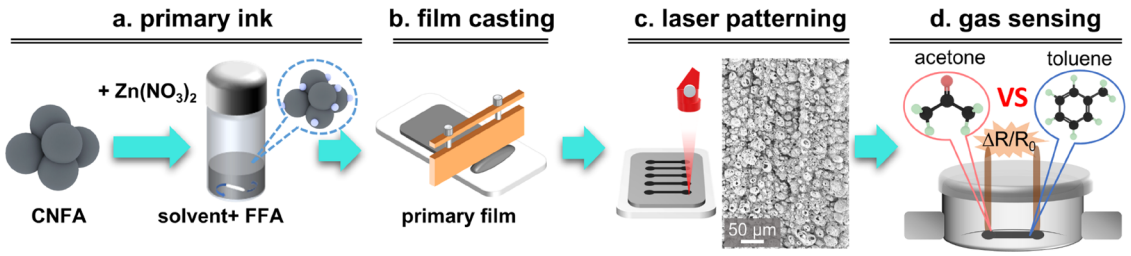

Figure 1. Illustration of the preparation process of the **LP-C/Zn** films and their characterization in a resistive gas sensing setup: (a) preparation of the primary ink; (b) film casting on the flexible PET substrate; (c) carbon laser patterning of the primary film and a representative SEM image of the resulting LP-C film; (d) electrochemical gas sensing cell used to characterize the resistive response of the LP-C sensor platforms in different gases inside the chamber.

abundancy, high cost of the raw material, and stability issues over time.[13] Operation temperatures of 200−400 °C make these materials highly sensitive; also, the associated devices are high energy-consuming and expensive. Alternative materials, such as carbon nanotubes and nanoparticle composites, are promising for room-temperature detection of VOCs; however, those typically come along with high production costs.[14]

New functional materials, such as hierarchical porous carbons, constitute interesting alternatives for utilization in everyday use or disposable sensor arrays.[15−17] Such porous carbon materials are usually prepared by the templated pyrolysis of organic precursors, incorporating functional active sites for enhancing selective analytes' interactions.[18] Major challenges that need to be tackled to prepare efficient porous carbon materials applicable for sensors are sensitivity, selectivity, stability, scalability, and flexibility.[19,20]

With modern laser pyrolysis, non-crude oil-based molecular precursors can be converted into conductive carbonized materials in the form of patterns on different substrates.[21−24] The resulting porous structures and their tunable conductivity makes these laser-patterned carbons (LP-C) interesting as active materials in resistive gas sensors.[25−33] This process avoids the inherent difficulties of processing carbonized materials into flexible conductive films and provides a scalable method for the production of stable resistive sensors. In particular, the possibility of tuning the properties of the carbons by simple modification of the primary ink formulas has demonstrated a significant enhancement of the sensitivity of LP-C.[34] That makes this process generally interesting for commercial applications.

Here, we report a simple method to incorporate selectivity elements into LP-Cs for tuning the surface properties of the LP-C sensing material, thereby for the selective detection of VOCs. Upon the addition of minor amounts of zinc nitrate ($Zn(NO_3)_2$) as a precursor, small ZnO nanoparticles are formed in situ during laser carbonization. The role of zinc oxide (ZnO) as an intermediary nanoscale porogen and graphitization agent has already been reported and successfully proven to increase the active surface area of porous carbon.[35−37] The high process temperatures in the upper layers support the direct evaporation of Zn formed during $Zn^+ \rightarrow ZnO \rightarrow Zn$ driven by the carbothermic reduction. In addition, we observe a variation in the surface relative to the Zn concentration. The concentration-dependent distribution of these graphitized domains and the increased surface area support the selectivity toward different VOCs. Moreover, the direct addition of readily prepared ZnO nanorods as a precursor leads to the formation of larger graphitic domains, supported by Raman spectroscopy, facilitating the preferential detection of VOCs that presumably adsorb to extended π-surfaces.

RESULTS AND DISCUSSION

Carbon laser patterning was performed according to a previously described protocol with several modifications.[34] A citric acid/urea-based carbon network-forming agent (CNFA) was thoroughly mixed with a film-forming agent (FFA) containing the solvent (ethylene glycol) and different amounts of $Zn(NO_3)_2$ were added (Figure 1a). The resulting viscous inks were doctor-bladed on PET substrates and dried to obtain films with a mean thickness of ca. 40 μm (Figure 1b). The films containing different amounts of $Zn(NO_3)_2$ are referred to as LP-C/Zn(**1−8**), with the number indicating the mass percentage of Zn with respect to the mass of CNFA (Table 1). The energy-dispersive X-ray analysis of the top-view primary films shows a homogeneous distribution of the zinc salt (Figure S1).

Table 1. Composition of the Investigated Samples

sample	CA/U(300) (mg)	$Zn(NO_3)_2{\cdot}6H_2O$ (mg)	ZnO nanorods (mg)	effective m_{Zn}(wt %)
LP-C/Zn(0)	200	0		0%
LP-C/Zn(1)	200	10		1%
LP-C/Zn(2)	200	20		2%
LP-C/Zn(4)	200	40		4%
LP-C/Zn(5)	200	60		5%
LP-C/Zn(6)	200	80		6%
LP-C/Zn(7)	200	100		7%
LP-C/Zn(8)	200	120		8%
LP-C/ZnO(2)	200		5	2%
LP-C/ZnO(7)	200		20	7%

Resistive patterns with dimensions of 5 × 0.5 mm were imprinted onto the films with a high-precision CO_2-laser engraver (see the Experimental Section). The laser parameters, i.e., scanning speed and power, were optimized to achieve a high degree of carbonization and high reproducibility in terms of conductivity. After laser patterning, the unexposed precursor film was rinsed off with H_2O. Subsequently, the sensor strips **LP-C/Zn** were tested as resistive sensor platforms to detect acetone and toluene at room temperature in a gas-flow cell (Figure 1d).

The topographical scanning electron microscopy (SEM) analyses of the **LP-C/Zn** films show a spore-like morphology for all zinc-containing samples (Figure S2). In contrast, the reference **LP-C/Zn(0)** is characterized by open hierarchical

https://doi.org/10.1021/acsanm.2c04348
ACS Appl. Nano Mater. 2023, 6, 966−975

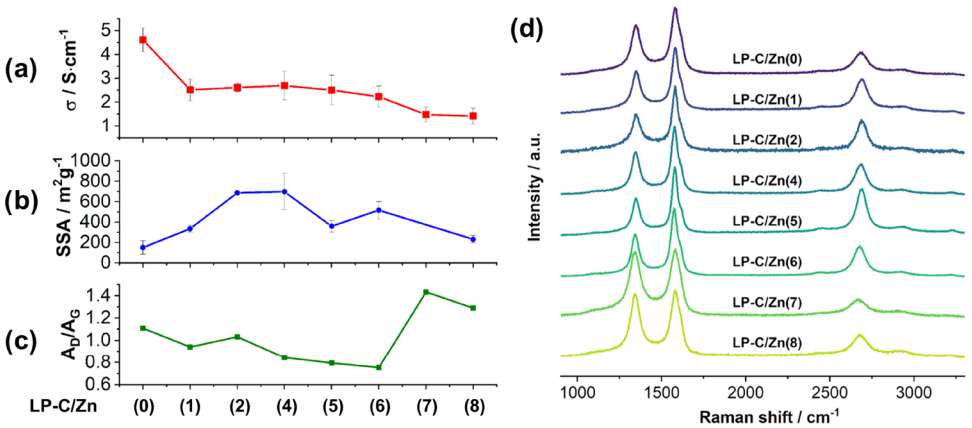

Figure 2. (a) Plot of sheet conductivity and (b) specific surface areas determined by the methylene blue adsorption method of the **LP-C/Zn** films; (c) A_D/A_G (area of the peak) ratio of **LP-C/Zn** films in the Raman spectra; (d) top-view Raman spectra of the **LP-C/Zn** films obtained with an excitation wavelength of 532 nm.

porous morphology (Figure S2). Notably, the spore-like character of the **LP-C/Zn** films is more pronounced for higher Zn concentrations (Figure S3).

A crucial property of resistive sensors is their conductivity. First, we tested the impact of the addition of zinc salt on the conductivity of the **LP-C/Zn** films by measuring the resistances of 30 sensor films of each as-prepared composite. A mean thickness of 40 μm was assumed for the determination of the sheet conductivity.[38] As shown in Figure 2a, the conductivity drops from 4.6 in reference to 2.5 S·cm^{-1} at 1 wt % Zn(**LP-C/Zn(1)**). Up to a concentration of 6 wt % Zn (**LP-C/Zn(6)**), the conductivity is on the same order, while another drop in conductivity to 1.4 S·cm^{-1} is observed at concentrations >7 wt % of Zn. Notably, at concentrations >8 wt %, the films tend to crack upon drying and eventually delaminate during the laser process. This quasilinear conductivity trend may be explained by the different factors that influence porous carbon materials: grain boundaries, particle sizes, atomic arrangement, and wettability, among others.[39]

The zinc salt is added with the intention of increasing the specific surface area (SSA) of **LP-C** by exploiting the carbothermic reduction of in situ-generated ZnO nanoparticles.[37] Due to the low mass density of the films, the characterization of the SSA using quantitative gas sorption techniques is intricate. Therefore, we utilized the methylene blue (MB) adsorption method to obtain insights into the evolution of the SSAs. It is noteworthy that the MB adsorption method is a liquid-based method and gives only indications about trends as it typically gives lower SSA values for nitrogen-containing carbons.[34] Moreover, potentially existing micropores are not accessible with this measurement method. However, the trend shows unambiguously higher SSAs upon the addition of zinc salt to the precursor films. The highest value is reached for a concentration of 4 wt % of Zn (**LP-C/Zn(4)**) with ∼700 m^2·g^{-1} (Figure 2b). For higher zinc concentrations, the SSAs decrease steadily.

Raman spectra of the **LP-C/Zn** and **LP-C/ZnO** series (Figures 2c,d and S4) exhibited an interesting top-layer analysis, complementing structural observations and correlated trends. All samples show features of a highly carbonized material with pronounced D- and G-bands at 1348 and 1578 cm^{-1}, respectively. Minor contributions from disordered and amorphous carbon at 1200 and 1470 cm^{-1}, designated as D4 and D3, were also observed and considered in the fittings.[40,41] A clear trend toward high graphitization with lower defect density is observed as the A_D/A_G ratio reduces from 1.1 to 0.75 between **LP-C/Zn(0)** and **LP-C/Zn(6)** (Figure 2c). This is concomitant with a decrease in the peak width of the 2D band at 2670 cm^{-1}, which indicates a higher stacking order of the graphite planes.[42] It is noteworthy that the Raman spectra were recorded at the surface of the films and are not ideally representative of the entire material. Due to the porous surface structure of laser-carbonized samples, the overall Raman spectroscopy characterization of PET film samples is challenging.

The general occurrence of a structural and chemical gradient in laser-carbonized materials prompted us to perform a cross-sectional transmission electron microscopy (TEM) analysis of the best-performing sensor films, **LP-C/Zn(5)**. To this end, the porous **LP-C/Zn(5)** sensor films were infiltrated and embedded in an epoxy resin and cut with a microtome into thin slices of ∼50 nm thickness.[38] An optical micrograph of the block face is presented in Figure 3a. Across the entire section, the films show a distinct porosity with visible pore sizes on the order of 5−10 μm represented in the scanning electron micrograph in Figure 3b.

The area in Figure 3b was further analyzed by energy-dispersive X-ray (EDX) analysis to obtain an overview of the chemical composition across the film. As demonstrated in previous studies, due to the direct exposure to the laser beam, the upper layer consists of porous turbostratic graphite with a highly crystalline structure (Figure 3c−e) and it is free of Zn.[38] In the lower layers, significant amounts of Zn were detected (Figure 3b). Scanning transmission electron microscopy−electron energy-loss spectroscopy (STEM-EELS) further confirmed the clear chemical and structural delineation between the highly graphitized top layer and the Zn/N-containing bottom layer (Figure 3c, right).

Depth-dependent laser thermal material conversion was evident based on the presence of highly ordered graphitic structures in the upper layer and ZnO in the lower part of the sensor, as detailed by the high-resolution TEM (HRTEM) images and the corresponding selected-area electron diffraction (SAED) patterns (Figure 3d−f).

These observations were corroborated by X-ray photoelectron spectroscopy (XPS) (Figure S5 and S6). In the C_{1s} energy region, the main peak at 284.4 eV is attributed to sp^2-

https://doi.org/10.1021/acsanm.2c04348
ACS Appl. Nano Mater. 2023, 6, 966−975

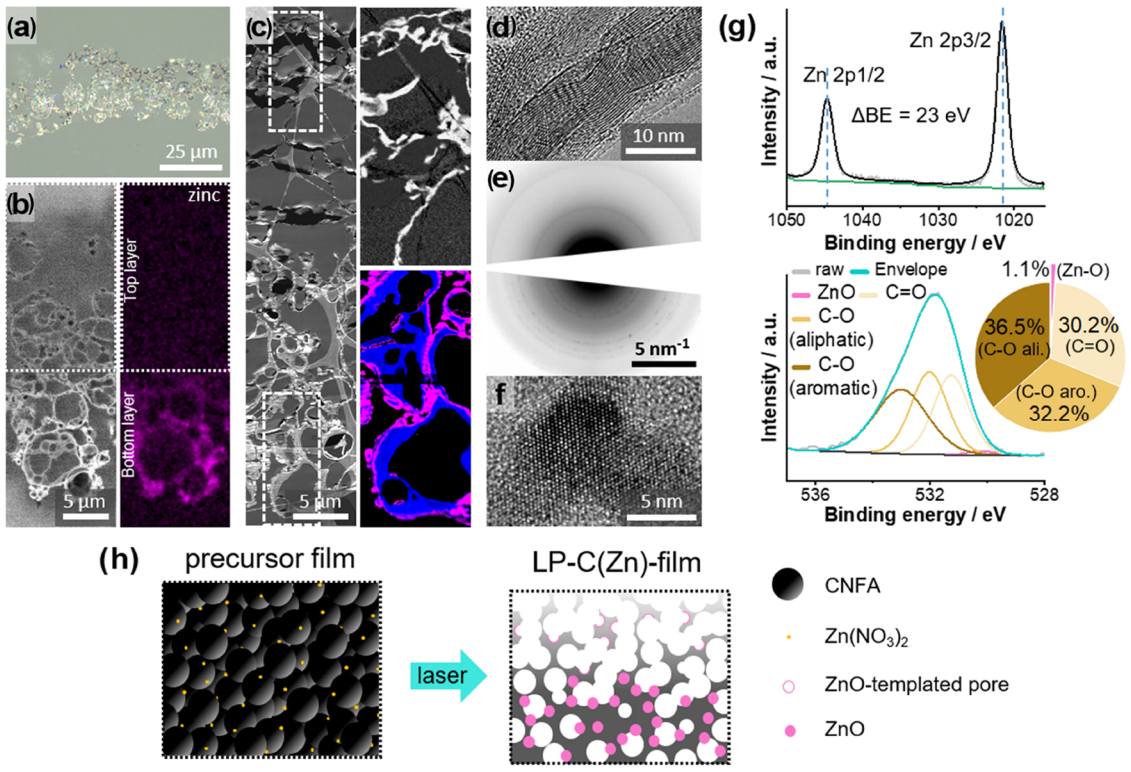

Figure 3. (a) Cross-sectional optical micrograph of **LP-C/Zn(5)**; (b) cross-sectional backscatter SEM micrograph with a correlated qualitative EDX element map of zinc (net intensities displayed); (c) cross-sectional TEM analyses of the sensor film: (left) the representative high-angle annular dark-field (HAADF)-STEM micrograph with uninfiltrated regions (black), epoxy resin (dark gray), and lacey TEM support film (light gray), (top right) graphitized carbon component in the upper layer identified by principle component analysis (PCA), (bottom right) N (blue) and Zn (purple) distribution in the bottom layer of the sensor; (d) exemplary HRTEM image of graphitized carbon in the upper region; (e) combined SAED pattern of graphitic domains in the top layer and ZnO in the bottom layer (logarithmic display); (f) exemplary HRTEM image of the ZnO nanoparticle in the lower layer; (g) XPS analysis of the **LP-C/Zn(5)** film surface: the XPS Zn 2p region (upper panel) and O 1s region with percentual peak distribution (lower panel); (h) proposed formation mechanism of the LP-C/Zn composite structure. $Zn(NO_3)_2$ is distributed among the CNFA particles in the precursor films. After laser carbonization, the in situ-generated ZnO nanoparticles catalyze the pore formation in the upper layer and remain in the lower layer.

carbon; the other minor peaks at 285.2, 286.0, 287.5, and 289.1 eV correspond to sp^3-carbon, C−N/C−O, C═N/C═O, and COOH, respectively. The N_{1s} region of the laser-carbonized films (**LP-C/Zn(*x*)**) was deconvoluted into three individual peaks maximizing at 399.0, 400.0, and 401.4 eV corresponding to pyridinic, pyrrolic, and graphitic nitrogen, respectively. For the primary films C/Zn(*x*), two additional peaks at 402.8 and 406.4 eV originate from NO_3^- and NO_2^-,[43] which are attributed to the addition of $Zn(NO_3)_2$ into the primary inks. The vanishing of these peaks confirms the decomposition of $Zn(NO_3)_2$ after laser patterning.

In the Zn_{2p} region (Figure 3g), the two intense peaks centered at binding energies of 1021.5 and 1044.5 eV are attributed to Zn $2p_{3/2}$ and Zn $2p_{1/2}$. The Zn 2p spectra of Zn oxide suffers from an overlap of Zn metal peaks, which makes it difficult to unambiguously determine the chemical state of Zn.[44,45] Nonetheless, the different binding energy of oxygen in metal oxides compared to organic compounds are reflected in the O_{1s} region[45] and can be used to identify the variety of ZnO surfaces.[46] The O_{1s} signal is deconvoluted into four peaks (Figure 3g), three major peaks centered at 531.2, 532.1, and 533.0 eV assigned to C═O, C−O (aliphatic), and C−O (aromatic),[47] respectively, along with a 0.8% peak contribution at 530.2 eV assigned to Zn−O.[46]

These results demonstrate the function of nanosized ZnO as a pore templating agent in the upper layers of the film during laser carbonization. The ZnO hard-templating effect based on the carbothermic reduction at different temperature stages occurs in situ within the time frame of milliseconds in a one-step process. As Figure 3h shows, the homogeneously distributed zinc salt ($Zn(NO_3)_2$) in the primary films forms ZnO nanoparticles upon elevating the reaction temperature during laser carbonization. When the laser-induced temperature reaches ~670 °C, ZnO is reduced to Zn according to the carbothermic reduction mechanism, during which carbon is oxidized to gaseous monoxide carbon ($CO_{(g)}$).[35] Remaining carbon is rearranged and recrystallized and thus forms highly graphitized domains (Figure 3c−e).[48] At temperatures above the boiling point of zinc (907 °C), liquid zinc evaporates. The high degree of graphitization and the absence of ZnO nanoparticles in the upper layers of the **LP-C/Zn** film indicate that the reaction temperatures are significantly higher than 907 °C. On the other hand, the presence of considerable amounts of ZnO nanoparticles and the rather amorphous character of carbon in the lower layers indicates lower reaction temperatures below 670 °C. Due to continuous evaporation of the carboneous matrix in the lower layer under those conditions, surface enrichment as well as the ripening of ZnO occurs (Figure 3c)

The increased SSA and the potential occurrence of ZnO-templated micropores is a great advantage for sensitivity toward the detection of gaseous analytes. We tested the

https://doi.org/10.1021/acsanm.2c04348
ACS Appl. Nano Mater. 2023, 6, 966−975

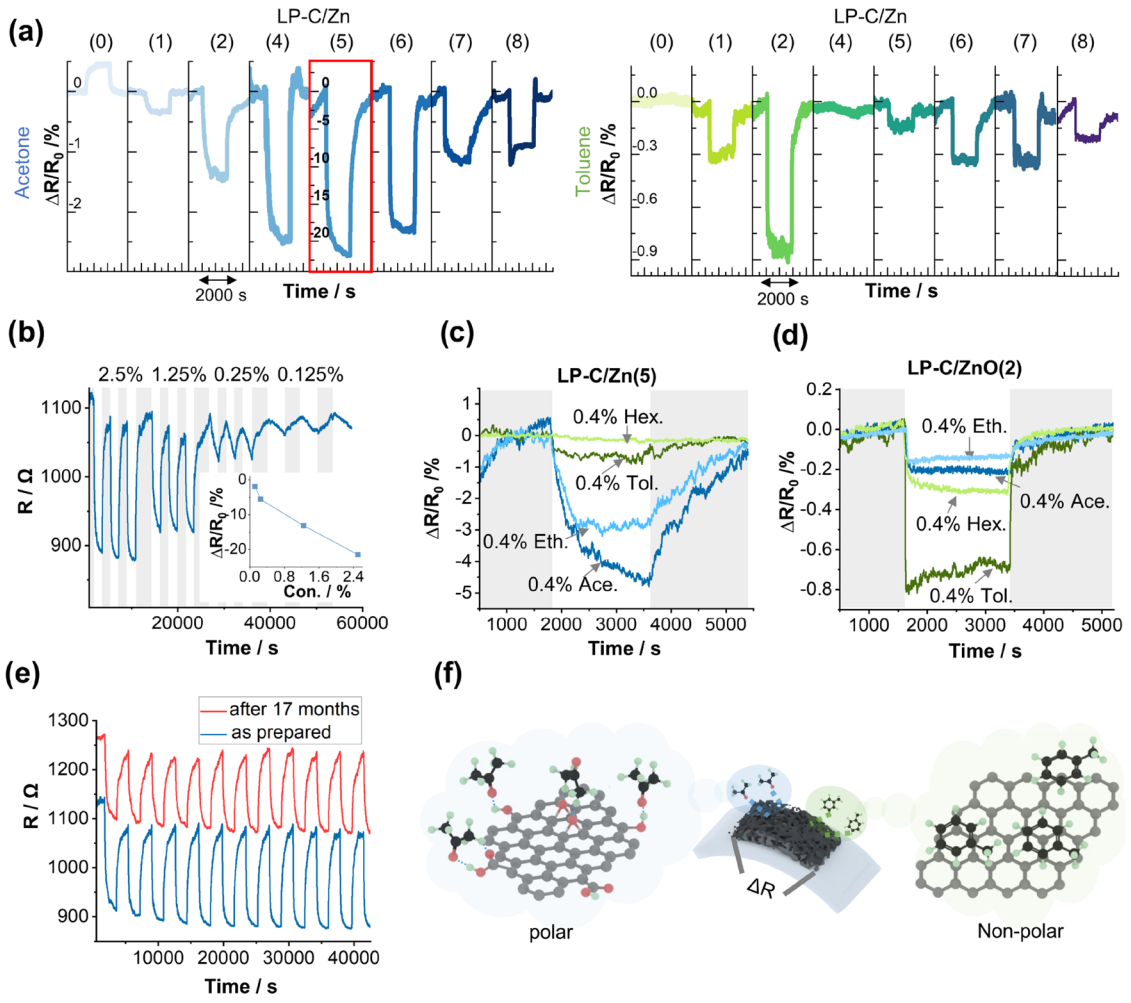

Figure 4. (a) Sensing response of the **LP-C/Zn** films toward 2.5% acetone (left) and 0.4% toluene (right); (b) resistive response of the LP-C/Zn(5) film toward 2.5, 1.25, 0.25, and 0.125% acetone (inserted is a plot of the sensitivity response $\Delta R/R_0$ vs CO_2 concentration) (gray area: 100% nitrogen sparged, nongray area: contains different concentrations of analytes); (c) resistive response of the LP-C/Zn(5) film toward 0.4% acetone, 0.4% ethanol, 0.4% toluene, and 0.4% hexane; (d) resistive response of the LP-C/ZnO(2) film toward 0.4% acetone, 0.4% ethanol, 0.4% toluene, and 0.4% hexane; (e) resistive response of LP-C/Zn(5) after 17 months toward 2.5% acetone in comparison to a freshly prepared sensor platform; (f) illustration of the adsorption mechanism of polar (acetone) and nonpolar (toluene) analytes to polar (oxygenated) or nonpolar (π-conjugated) surfaces.

resistive response of each sensor composite film toward the exposure of representative polar and nonpolar VOCs, namely, acetone and toluene.[49] Figure 4a,b shows the response of each sensor film with different Zn content toward the test analytes. All samples, except for the reference without Zn, show a clear negative response upon exposure to acetone. The response to acetone rises with the Zn content and reaches a peak for the sample with 5 wt % of Zn (**LP-C/Zn(5)**, e.g., $\Delta R/R_0$ = −21.5% at 2.5% acetone). In comparison to the samples with slightly less or more Zn, **LP-C/Zn(4)** and **LP-C/Zn(6)**, the response is drastically low by one order of magnitude. Also, the response toward the nonpolar analyte, toluene, is enhanced in the zinc-containing films, although the trends are not as clear in this case. In fact, the reference film free of zinc shows no response toward toluene whatsoever. The highest response of $\Delta R/R_0$ = −0.9% to the exposure of 0.4% toluene is observed for **LP-C/Zn(2)**. Samples **LP-C/Zn(4)** and **(5)** give lower specific responses for toluene and again **LP-C/Zn(6)** gives a decent response. The drastic increase in the response at **LP-C/Zn(5)** is likely due to the formation of high amounts of micropores in this concentration regime.

The response depends on the analyte concentration, as shown in Figure 4b. A reasonable response of $\Delta R/R_0$ = −1.9% at relatively low analyte concentrations of 0.125% (1250 ppm) acetone is detected. With regard to selectivity, the sample **LP-C/Zn(5)** shows the highest affinity and selectivity to polar VOCs, e.g., $\Delta R/R$ = −4.7% at 0.4% acetone and $\Delta R/R$ = −3.0% at 0.4% ethanol (Figure 4c), while it shows little response to nonpolar toluene and hexane at the same concentration. This response pattern indicates physisorption based on different binding mechanisms of polar and nonpolar analytes. In addition, in stability testing of up to 24 h, we observed that sensitivity remained nearly constant over time Figure S13.

In previous works, we demonstrated the polar character of the LP-C surface due to an abundance of oxygen functional groups.[25] For polar analytes such as acetone, two physisorption scenarios with polar sites on the surface need to be considered: hydrogen-bonding and van der Waals interactions. Considering that the latter consist of contributions from dipole, induction, and dispersion forces, the adsorption of acetone to the LP-C surface is mostly attributed to dipole−dipole interactions.[50−52]

https://doi.org/10.1021/acsanm.2c04348
ACS Appl. Nano Mater. 2023, 6, 966−975

For toluene, on the other hand, dispersion forces or $\pi-\pi$ stacking are implicit (Figure 4f).[53,54] Taking these fundamental molecular interactions into consideration, the sorption selectivity in the different samples is attributed to the surface properties of LP-C. Generally, the surface of LP-C is polar and, therefore, sensitive to polar analytes. On the one hand, the hard-templating effect of ZnO nanoparticles promotes the formation of small pores and eventually micropores, which enhances the response toward acetone. On the other hand, the graphitization-catalyzing effect of ZnO during carbothermic reduction promotes the formation of an extended π-surface, which enhances the sensitivity toward toluene.

To demonstrate the feasibility of the suggested mechanism, we also tested the sensing performance of films prepared with presynthesized ZnO nanorods with average sizes of ~2 μm as precursors. These sensor films are named LP-C/ZnO(x), with x indicating the mass percentage of Zn in the precursor inks. The rhombus-like ZnO nanorods were randomly distributed in the primary film and underwent the same in situ carbothermic reduction process during laser patterning (Figure S7). Due to their significantly larger size, the ZnO nanorods are expected to support the formation of larger graphitic domains in the upper layers of the LP-C films. Indeed, the SEM images show an open porous but nonsporulated morphology (Figure S8). After the laser patterning process, it can be seen from the EDX mapping analysis (Figure S9) that some of the ZnO nanorods or their debris are still distributed on the surface of the sensor films, but their shapes are enlarged or even broken due to the expansion effect. Regarding the characteristics in terms of graphitization (Figure S10) and electrical conductivity, the two representative samples, **LP-C/ZnO(2)** and **LP-C/ZnO(7)**, show the same trends as the samples from the LP-C/Zn(x) series. In comparison to the reference **LP-C**, the conductivity of the LP-C/Zn(x) series decreased (Figure S11). However, we observe a slight increase in conductivity with the amount of ZnO nanorods added. We assume that the enhanced formation of graphitized domains supports electrical conductivity.

In general, for the samples prepared with presynthesized ZnO nanorods, upon laser patterning, the ZnO nanorods in the upper layer are partially reduced to Zn to catalyze the graphitization of surrounding carbon and then evaporate. Parts of the ZnO nanorods accumulate in the intermediate region of the bottom and top layer, whereas particle ripening is hindered in the lowest region due to preoxidation and lower temperatures (Figure S12).

In fact, the sample containing 2 wt % Zn, i.e., **LP-C/ZnO(2)**, shows a significantly higher selectivity toward 0.4% toluene and hexane with a response of $\Delta R/R_0 = -0.8$ and 0.3%, respectively, than to acetone ($\Delta R/R_0 = -0.2\%$ at 0.4% acetone) and ethanol ($\Delta R/R_0 = -0.13\%$ at 0.4% ethanol) (Figure 4d). Furthermore, as shown in Figure S14, **LP-C/ZnO(2)** shows good stability over time. A reasonable response of $\Delta R/R_0 = 0.14\%$ at a relatively low analyte concentration of 0.4% (400 ppm) toluene is detected.

At last, we tested the long-term stability of the sensor platforms. We stored the sensor film **LP-C/Zn(5)** under ambient conditions for 17 months and tested it under the same 2.5% acetone. Comparing the freshly prepared sample, the aged sample shows a slightly lower response of $\Delta R/R_0 = -12.7\%$ (Figure 4e). The reduced sensitivity is attributed to the increased base resistance, which may be due to a partial oxidation/degradation of the surface groups on the sensor films.[34] Moreover, we tested the sensor films at different ambient temperatures (Figure S15) and at room temperature (25 °C), which shows the highest resistance response. On the other hand, a stable and fast response, even at an ambient temperature of 60 °C, is observed.

CONCLUSIONS

The carbothermic reduction initiated by the presence of ZnO nanoparticles during laser carbonization was studied. ZnO nanoparticles were generated in situ from $Zn(NO_3)_2$ that was added to the primary films. A comprehensive investigation of the chemical composition and microscopic morphology by XPS and cross-sectional HRTEM reveals a heterogeneous gradient profile due to the induced temperature gradient during laser carbonization. Two positive effects were observed: (1) A significant increase in the active surface area due to the hard-templating effect of the ZnO and (2) the catalysis of graphitization around the ZnO nanoparticles. By careful selection of the initial $Zn(NO_3)_2$ concentration, the surface structure of LP-C can be tuned in terms of surface properties, predominantly porosity and polarity. Thereby, a drastically enhanced response toward different VOCs was achieved in resistive sensing experiments. Notably, electronic effects on the sensitivity were not specifically tested. At a concentration of 5 wt % Zn, the response toward acetone was increased by 43× with respect to the reference ($\Delta R/R_0 = -21.5\%$ at 2.5% acetone), which is attributed to a significantly higher porosity. The surface polarity was considered an important factor. Using presynthesized ZnO nanorods as additives, large graphitic domains were obtained after laser carbonization, which present extended nonpolar π-surfaces as active sites. Thereby, a response with a high selectivity toward toluene ($\Delta R/R_0 = -0.8\%$ at 0.4% toluene) was achieved. The herein-presented advancements in laser carbonization may inspire the development of smart sensor arrays based on a simple materials processing technology. Yet, the increase of the sensitivity to the low ppm level and the decrease in the response times still remain a challenge.

EXPERIMENTAL SECTION

Chemicals. Citric acid (99%, Sigma-Aldrich), urea (>99.3%, Alfa Aesar), zinc nitrate hexahydrate ($Zn(NO_3)_2{\cdot}6H_2O$, standard grade, Thermo Fisher Scientific GmbH), ethylene glycol (≥99.7%, AnalaR Normapur, VWR chemicals), poly(vinylpyrrolidone) (average mol wt. 10,000, Sigma-Aldrich), acetone (≥99.8% HPLC grade, Thermo Fisher Scientific GmbH), and toluene (≥99.8% HPLC grade, Thermo Fisher Scientific GmbH) were used as received.

Substrate. Melinex sheets (PET substrates) with a thickness of 170 μm were obtained from Plano GmbH.

Preparation of the CNFA. The CNFA was prepared following a protocol described elsewhere.[21] Briefly, citric acid and urea were mixed in equivalent weight proportions in a quartz crucible. The mixture was annealed at 300 °C in a tube furnace (RHTC 80/450/15, Nabertherm) for 2 h with a heating rate of 3.11 K·min^{-1}. After annealing, the reaction products were ground by ball milling (PM 100, Retsch) for 1 h at 600 rpm. The resulting black powder is named CA/U(300).

Preparation of the ZnO Nanorods. $Zn(NO_3)_2$ (3g) and NaOH (0.8 g) were added to 500 ml of H_2O. The resulting white suspension was partially added to the microwave vessel. Then, using a microwave power of 200 W to reach the reaction temperature of 150 °C held for 5 min. The reaction product mixture was centrifuged to remove the soluble part. The precipitate was washed with ethanol and centrifuged; the washing process was repeated 2 times. The obtained white solid ZnO nanorods were dried overnight at 70 °C in the oven.

https://doi.org/10.1021/acsanm.2c04348
ACS Appl. Nano Mater. 2023, 6, 966−975

Preparation of the Primary Films. Poly(vinylpyrrolidone) (PVP) (film-forming agent) was dissolved in ethylene glycol (EtGly) to obtain a 0.2 g·mL^{-1} solution (PVP/EtGly). Solutions with eight different concentrations of zinc nitrate ($Zn(NO_3)_2$) ranging from 0 to 0.6 mg·mL^{-1} were prepared, referred to as LP-C/Zn(**1**−**8**), where the number represents the amount of Zn in wt % (Table 1). CA/U(300) was then added and stirred for 24 h to obtain a viscous suspension with a concentration of 0.8 g·mL^{-1}. All concentrations are given with respect to the volume of the solvent. A drop of the ink was applied onto the substrate and the ink was doctor bladed with a blade distance of 300 μm. Ethylene glycol was then evaporated at 80 °C on a precision hotplate (PZ2860-SR, Gestigkeit GmbH) overnight to obtain films with a thickness of 40 μm. The thickness was determined with a digital micrometer or cross-sectional SEM.

Laser Carbonization. A high-precision laser engraver setup (Speedy 100, Trotec) equipped with a 60 W CO_2-laser (λ = 10.6 ± 0.03 μm) was used for laser carbonization. Focusing was achieved with a 2.5 in. focus lens providing a focal depth of ∼3 mm and a focus diameter of 170 μm. The scanning speed v', generically given in percentage, was converted into s·m^{-1}. The effective output power P of the laser was measured with a Solo 2 (Gentec Electro-Optics) power meter. The resulting energy input per distance (or fluence) F in J·m^{-1} in the vector mode onto the film is given by

$$F = P \cdot v'$$

For the experiments, the laser settings were adjusted to meet the requirements of the films according to Table 2. Each laser pattern consists of five parallel laser lines with a length of 5 mm and a line separation of 0.1 mm to obtain a sensor film.

Table 2. Laser Parameters Used in the Experiments to Fit the Film Thickness

thickness(μm)	power% (generic)	power(W)	speed% (generic)	speed (s·m^{-1})	fluence (J·m^{-1})
20	2.0	1.02	0.6	98	99.5

VOCs Sensing. The sensor experiments were performed in a gas-flow cell (V_{cell} ≈ 0.1 L). The ends of the sensor films were connected to two electrode pins and electrically characterized with an impedance unit (Solartron 1287 potentiostat in combination with a SI 1260 impedance unit) at a frequency of 1000 Hz and in AC conditions applying a current of 0.05 mA. The gas flow was controlled with a set of three mass-flow controllers (GF040 from Brooks instruments). The total gas flow was set to 1 L·min^{-1}. Cycles of 30 min between pure nitrogen and the analyte (acetone or toluene) were performed. To this end, a defined volume of the total flow was passed through a reservoir of the respective liquid VOCs. The final concentration of the analyte was approximated using the ideal gas law based on the vapor pressure of the VOC.

Characterization. Conductivity measurements were carried out by connecting the ends of each sensor film with silver ink and measuring the resistance with a four-point geometry using an RS PRO2 RSDM3055A digital multimeter.

Specific surface area measurements were performed using the methylene blue adsorption method.[55−57] LP-C films of size 2 × 4 cm^2 were printed on PET sheets. Pieces of ∼0.5 × 1 cm^2 with the laser-patterned films on top were balanced and then immersed into defined solutions of methylene blue (9.5 × 10^{-5} M) to disperse the LP-C film in the solution. To determine the mass of the film, the PET substrate was removed and weighted. The LP-C dispersion in the MB solution was stirred for 24 h and then centrifuged. The amount of adsorbed MB was determined by measuring the absorbance of the supernatant with respect to a reference solution. An area of 1.35 nm^2 per molecule MB is assumed. As a reference, the same mass of activated carbon was used (1269 m^2·g^{-1}). The standard error was determined by the standard deviation of six values obtained from six measurements.

Raman spectra were obtained with a confocal Raman microscope (alpha300, WITec, Germany) equipped with a piezo-scanner (P-500, Physik Instrumente, Karlsruhe, Germany). The laser, λ = 532 nm, was focused on the samples through a 50× objective. The laser power on the sample was set to 5.0 mW.

Cross-sectional preparation of LP-C for electron microscopic analyses was performed using a Leica EM UC7 ultramicrotome. Therefore, sensor strips were embedded in epoxy resin (Araldite 502, Science Services, Germany) to enable sectioning by infiltrating the highly porous heterostructures. Curing of the epoxy resin was carried out overnight at 60 °C. A diamond knife (DiATOME 45° trim knife) was utilized to trim a trapezoid-shaped block face which subsequently was cut with a DiATOME 45° ultrasonic diamond knife to obtain cross-sectional TEM samples with minimal compression. The floating sections (deionized water) were transferred onto lacey carbon TEM grids (Plano AG) to provide sufficient support. Analysis by optical microscopy (OM) and environmental SEM was conducted with the resulting block face.

Top-view scanning electron microscopy was performed on a Zeiss LEO 1550-Gemini system (acceleration voltage: 3 to 10 kV). An Oxford Instruments X-MAX 80 mm^2 detector was used to collect the SEM-EDX data. Cross-sectional imaging with back-scattered electrons and EDXS elemental mapping of the epoxy-embedded samples (microtomy block surface) were performed using an environmental FEI Quanta 250 FEG-SEM. An Apollo XL SDD detector was used to obtain EDXS elemental maps at 5 keV primary electron energy as a compromise between count rate and lateral resolution. To reduce sample charging, the instrument was operated at a N_2 pressure of 70−90 Pa.

Transmission electron microscopy was performed using a Thermo Fisher FEI Talos F200X operated at 200 kV. Besides an XFEG high-brightness gun and a large-area Super-X EDXS detector, the instrument is equipped with a Gatan Continuum ER spectrometer for electron energy-loss spectroscopy. Bright-field imaging, selected-area electron diffraction, high-resolution TEM, and high-angle annular dark-field scanning TEM were utilized to analyze the structure and morphology of the LP-C microtomic cross-sections. Dual EELS mappings with an energy range of the core-loss spectra of 200−800 eV (dispersion 0.3 eV/channel) for the upper region and 200−1800 eV (dispersion 0.75 eV/channel) for the lower region were acquired to include the ionization edges of C, N, O, and Zn at around 285, 400, 532, and 1020 eV, respectively.

To visualize the distribution of graphitized carbon in the top layer as well as the N and Zn distributions of the bottom layer, principal component analysis (PCA) was employed to analyze the STEM-EELS data. PCA was used as implemented in the Gatan Microscopy Suite (GMS) version 3.4.[58] (The details of the data evaluation are described in our previous study).

X-ray photoelectron spectroscopy was acquired using a Kratos Axis SUPRA using monochromated Al kα (1486.69 eV) X-rays at 15 mA emission and 12 kV HT (180W) and a spot size/analysis area of 700 × 300 μm^2. The instrument was calibrated to gold metal Au 4f (83.95 eV) and dispersion was adjusted to give a BE of 932.6 eV for the Cu 2p3/2 line of metallic copper. The Ag 3d5/2 line FWHM at 10 eV pass energy was 0.544 eV. The source resolution for monochromatic Al Kα X-rays is ∼0.3 eV. The instrumental resolution was determined to be 0.29 eV at 10 eV pass energy using the Fermi edge of the valence band for metallic silver. Resolution with the charge compensation system on <1.33 eV FWHM on PTFE. High-resolution spectra were obtained using a pass energy of 20 eV, step size of 0.1 eV, and sweep time of 60 s, resulting in a line width of 0.696 eV for Au 4f7/2. Survey spectra were obtained using a pass energy of 160 eV. Charge neutralization was achieved using an electron flood gun with the filament current = 0.4 A, charge balance = 2 V, and filament bias = 4.2 V. Successful neutralization was adjudged by analyzing the C 1s region wherein a sharp peak with no lower BE structure was obtained. Spectra have been charge corrected to the main line of the carbon 1s spectrum (adventitious carbon) set to 284.8 eV. All data was recorded at a base pressure of below 9 × 10-9 Torr and a room temperature of

https://doi.org/10.1021/acsanm.2c04348
ACS Appl. Nano Mater. 2023, 6, 966−975

294 K. Data was analyzed using CasaXPS v2.3.19PR1.0. Peaks were fit with a Shirley background prior to component analysis.

■ ASSOCIATED CONTENT

Data Availability Statement

The datasets generated during and/or analyzed during the current study are available from the corresponding author upon reasonable request.

Supporting Information

The Supporting Information is available free of charge at https://pubs.acs.org/doi/10.1021/acsanm.2c04348.

Energy-dispersive X-ray analysis; scanning electron microscopy; Raman spectroscopic analysis; X-ray photoelectron spectroscopic analysis; X-ray photoelectron spectroscopic analysis; electrical conductivity measurements; cross-sectional microscopic analysis; and sensor performance (PDF)

■ AUTHOR INFORMATION

Corresponding Author

Volker Strauss − *Max Planck Institut für Kolloid- und Grenzflächenforschung, 14476 Potsdam, Germany;* orcid.org/0000-0003-2619-6841; Email: volker.strauss@mpikg.mpg.de

Authors

Huize Wang − *Max Planck Institut für Kolloid- und Grenzflächenforschung, 14476 Potsdam, Germany*

Pablo Jiménez-Calvo − *Max Planck Institut für Kolloid- und Grenzflächenforschung, 14476 Potsdam, Germany;* orcid.org/0000-0002-9826-6995

Marco Hepp − *Micro- and Nanoanalytics Group, University of Siegen, 57076 Siegen, Germany;* orcid.org/0000-0002-5811-8672

Mark Andrew Isaacs − *Harwell XPS, Research Complex at Harwell, Rutherford Appleton Laboratories, Didcot OX11 0FA, U.K.;* orcid.org/0000-0002-0335-4272

Charles Otieno Ogolla − *Micro- and Nanoanalytics Group, University of Siegen, 57076 Siegen, Germany*

Ines Below-Lutz − *Max Planck Institut für Kolloid- und Grenzflächenforschung, 14476 Potsdam, Germany*

Benjamin Butz − *Micro- and Nanoanalytics Group, University of Siegen, 57076 Siegen, Germany;* orcid.org/0000-0002-9744-3419

Complete contact information is available at: https://pubs.acs.org/10.1021/acsanm.2c04348

Author Contributions

H.W.: investigation, methodology, validation, formal analysis, and writing—original draft; P.J.-C.: investigation, methodology, validation, formal analysis, and writing—original draft; M.H.: investigation, methodology, validation, formal analysis, and writing—original draft; M.I.: investigation, methodology, validation, and writing—original draft; I.B.-L.: investigation; B.B.: supervision, methodology, validation, and writing—review & editing; and V.S.: conceptualization, methodology, validation, writing—original draft, writing—review & editing, supervision, and project administration.

Funding

Open access funded by Max Planck Society.

Notes

The authors declare no competing financial interest.

The authors declare that they have no known competing financial interests or personal relationships that could have appeared to influence the work reported in this paper.

■ ACKNOWLEDGMENTS

The authors are grateful for financial support from the Fonds der Chemischen Industrie and the Max Planck Society. The authors thank Klaus Bienert for help with the gas sensing setup. Open access funding was enabled and organized by the German Projekt DEAL. The X-ray photoelectron (XPS) data collection was performed at the EPSRC National Facility for XPS ("HarwellXPS"), operated by Cardiff University and UCL, under Contract No. PR16195. Part of this work was performed at the DFG-funded Micro-and Nanoanalytics Facility (MNaF) of the University of Siegen (INST 221/131-1) utilizing its major TEM instrument FEI Talos F200X (DFG INST 221/93-1, DFG INST 221/126-1) and sample preparation equipment.

■ REFERENCES

(1) Environmental Protection Agency. *Technical Overview of Volatile Organic Compounds*, 2017.

(2) Szulczyński, B.; Gębicki, J. Currently Commercially Available Chemical Sensors Employed for Detection of Volatile Organic Compounds in Outdoor and Indoor Air. *Environments* **2017**, *4*, No. 21.

(3) Spinelle, L.; Gerboles, M.; Kok, G.; Persijn, S.; Sauerwald, T. Review of Portable and Low-Cost Sensors for the Ambient Air Monitoring of Benzene and Other Volatile Organic Compounds. *Sensors* **2017**, *17*, No. 1520.

(4) Saasa, V.; Malwela, T.; Beukes, M.; Mokgotho, M.; Liu, C.-P.; Mwakikunga, B. Sensing Technologies for Detection of Acetone in Human Breath for Diabetes Diagnosis and Monitoring. *Diagnostics* **2018**, *8*, No. 12.

(5) Meng, F.; Shi, X.; Yuan, Z.; Ji, H.; Qin, W.; Shen, Y.; Xing, C. Detection of Four Alcohol Homologue Gases by ZnO Gas Sensor in Dynamic Interval Temperature Modulation Mode. *Sens. Actuators, B* **2022**, *350*, No. 130867.

(6) Probert, C.; Ahmed, I.; Khalid, T.; Smith, S.; Ratcliffe, N. Volatile Organic Compounds as Diagnostic Biomarkers in Gastrointestinal and Liver Diseases. *J. Gastrointest. Liver Dis.* **2009**, *18*, 337−343.

(7) Das, S.; Pal, M. Review—Non-Invasive Monitoring of Human Health by Exhaled Breath Analysis: A Comprehensive Review. *J. Electrochem. Soc.* **2020**, *167*, No. 037562.

(8) Wilson, A. D. Application of Electronic-Nose Technologies and VOC-Biomarkers for the Noninvasive Early Diagnosis of Gastrointestinal Diseases. *Sensors* **2018**, *18*, No. 2613.

(9) Hayasaka, T.; Lin, A.; Copa, V. C.; Lopez, L. P.; Loberternos, R. A.; Ballesteros, L. I. M.; Kubota, Y.; Liu, Y.; Salvador, A. A.; Lin, L. An Electronic Nose Using a Single Graphene FET and Machine Learning for Water, Methanol, and Ethanol. *Microsyst. Nanoeng.* **2020**, *6*, No. 50.

(10) Guo, L.; Wang, T.; Wu, Z.; Wang, J.; Wang, M.; Cui, Z.; Ji, S.; Cai, J.; Xu, C.; Chen, X. Portable Food-Freshness Prediction Platform Based on Colorimetric Barcode Combinatorics and Deep Convolutional Neural Networks. *Adv. Mater.* **2020**, *32*, No. 2004805.

(11) https://smart-nanotubes.com/; date of access: December 06, 2022.

(12) Ji, H.; Mi, C.; Yuan, Z.; Liu, Y.; Zhu, H.; Meng, F. Multi-Component Gas Detection Method via Dynamic Temperature Modulation Measurements Based on Semiconductor Gas Sensor. *IEEE Trans. Ind. Electron.* **2022**, 1−10.

(13) Wang, C.; Yin, L.; Zhang, L.; Xiang, D.; Gao, R. Metal Oxide Gas Sensors: Sensitivity and Influencing Factors. *Sensors* **2010**, *10*, 2088−2106.

(14) Andre, R. S.; Sanfelice, R. C.; Pavinatto, A.; Mattoso, L. H. C.; Correa, D. S. Hybrid Nanomaterials Designed for Volatile Organic Compounds Sensors: A Review. *Mater. Des.* **2018**, *156*, 154−166.
(15) Zhang, W.; Li, G.; Yin, H.; Zhao, K.; Zhao, H.; An, T. Adsorption and Desorption Mechanism of Aromatic VOCs onto Porous Carbon Adsorbents for Emission Control and Resource Recovery: Recent Progress and Challenges. *Environ. Sci.: Nano* **2022**, *9*, 81−104.
(16) Kante, K.; Florent, M.; Temirgaliyeva, A.; Lesbayev, B.; Bandosz, T. J. Exploring Resistance Changes of Porous Carbon upon Physical Adsorption of VOCs. *Carbon* **2019**, *146*, 568−571.
(17) Jiao, Y.; Cho, S. W.; Lee, S.; Kim, S. H.; Jeon, S.-Y.; Hur, K.; Yoon, S. M.; Moon, M.-W.; Wang, A. A Hierarchically Porous Carbon Fabric for Highly Sensitive Electrochemical Sensors. *Adv. Eng. Mater.* **2018**, *20*, No. 1700608.
(18) Zhang, X.; Gao, B.; Creamer, A. E.; Cao, C.; Li, Y. Adsorption of VOCs onto Engineered Carbon Materials: A Review. *J. Hazard. Mater.* **2017**, *338*, 102−123.
(19) Mulmi, S.; Thangadurai, V. Editors' Choice—Review—Solid-State Electrochemical Carbon Dioxide Sensors: Fundamentals, Materials and Applications. *J. Electrochem. Soc.* **2020**, *167*, No. 037567.
(20) Zhao, X.-H.; Ma, S.-N.; Long, H.; Yuan, H.; Tang, C. Y.; Cheng, P. K.; Tsang, Y. H. Multifunctional Sensor Based on Porous Carbon Derived from Metal−Organic Frameworks for Real Time Health Monitoring. *ACS Appl. Mater. Interfaces* **2018**, *10*, 3986−3993.
(21) Delacroix, S.; Wang, H.; Heil, T.; Strauss, V. Laser-Induced Carbonization of Natural Organic Precursors for Flexible Electronics. *Adv. Electron. Mater.* **2020**, *6*, No. 2000463.
(22) Edberg, J.; Brooke, R.; Hosseinaei, O.; Fall, A.; Wijeratne, K.; Sandberg, M. Laser-Induced Graphitization of a Forest-Based Ink for Use in Flexible and Printed Electronics. *npj Flexible Electron.* **2020**, *4*, No. 17.
(23) Mohazzab, B. F.; Jaleh, B.; Nasrollahzadeh, M.; Khazalpour, S.; Sajjadi, M.; Varma, R. S. Upgraded Valorization of Biowaste: Laser-Assisted Synthesis of Pd/Calcium Lignosulfonate Nanocomposite for Hydrogen Storage and Environmental Remediation. *ACS Omega* **2020**, *5*, 5888−5899.
(24) Yuan, M.; Luo, F.; Rao, Y.; Wang, Y.; Yu, J.; Li, H.; Chen, X. Laser Synthesis of Superhydrophilic O/S Co-Doped Porous Graphene Derived from Sodium Lignosulfonate for Enhanced Microsupercapacitors. *J. Power Sources* **2021**, *513*, No. 230558.
(25) Delacroix, S.; Zieleniewska, A.; Ferguson, A. J.; Blackburn, J. L.; Ronneberger, S.; Loeffler, F. F.; Strauss, V. Using Carbon Laser Patterning to Produce Flexible, Metal-Free Humidity Sensors. *ACS Appl. Electron. Mater.* **2020**, *2*, 4146−4154.
(26) Sharma, S.; Ganeshan, S. K.; Pattnaik, P. K.; Kanungo, S.; Chappanda, K. N. Laser Induced Flexible Graphene Electrodes for Electrochemical Sensing of Hydrazine. *Mater. Lett.* **2020**, *262*, No. 127150.
(27) Wan, Z.; Nguyen, N.-T.; Gao, Y.; Li, Q. Laser Induced Graphene for Biosensors. *Sustainable Mater. Technol.* **2020**, *25*, No. e00205.
(28) Watanabe, A.; Cai, J.; Ogawa, S.; Aoyagi, E.; Ito, S.Laser Reduced Graphene Oxide-Based Interdigitated Electrode for Sensor Applications. In *Laser-based Micro- and Nanoprocessing XIII*; Klotzbach, U.; Kling, R.; Watanabe, A., Eds.; SPIE, 2019; p 38.
(29) Luo, J.; Yao, Y.; Duan, X.; Liu, T. Force and Humidity Dual Sensors Fabricated by Laser Writing on Polyimide/Paper Bilayer Structure for Pulse and Respiration Monitoring. *J. Mater. Chem. C* **2018**, *6*, 4727−4736.
(30) Zhu, C.; Tao, L.-Q.; Wang, Y.; Zheng, K.; Yu, J.; L, X.; Chen, X.; Huang, Y. Graphene Oxide Humidity Sensor with Laser-Induced Graphene Porous Electrodes. *Sens. Actuators, B* **2020**, *325*, No. 128790.
(31) Rahimi, R.; Ochoa, M.; Ziaie, B. Direct Laser Writing of Porous-Carbon/Silver Nanocomposite for Flexible Electronics. *ACS Appl. Mater. Interfaces* **2016**, *8*, 16907−16913.
(32) Nam, K.-H.; Abdulhafez, M.; Castagnola, E.; Tomaraei, G. N.; Cui, X. T.; Bedewy, M. Laser Direct Write of Heteroatom-Doped Graphene on Molecularly Controlled Polyimides for Electrochemical Biosensors with Nanomolar Sensitivity. *Carbon* **2022**, *188*, 209−219.
(33) Stanford, M. G.; Yang, K.; Chyan, Y.; Kittrell, C.; Tour, J. M. Laser-Induced Graphene for Flexible and Embeddable Gas Sensors. *ACS Nano* **2019**, *13*, 3474−3482.
(34) Wang, H.; Delacroix, S.; Zieleniewska, A.; Hou, J.; Tarakina, N. V.; Cruz, D.; Lauermann, I.; Ferguson, A. J.; Blackburn, J. L.; Strauss, V. In Situ Synthesis of Molybdenum Carbide Nanoparticles Incorporated into Laser-Patterned Nitrogen-Doped Carbon for Room Temperature VOC Sensing. *Adv. Funct. Mater.* **2021**, *31*, No. 2104061.
(35) Yan, B.; Zheng, J.; Wang, F.; Zhao, L.; Zhang, Q.; Xu, W.; He, S. Review on Porous Carbon Materials Engineered by ZnO Templates: Design, Synthesis and Capacitance Performance. *Mater. Des.* **2021**, *201*, No. 109518.
(36) Yan, R.; Leus, K.; Hofmann, J. P.; Antonietti, M.; Oschatz, M. Porous Nitrogen-Doped Carbon/Carbon Nanocomposite Electrodes Enable Sodium Ion Capacitors with High Capacity and Rate Capability. *Nano Energy* **2020**, *67*, No. 104240.
(37) Strubel, P.; Thieme, S.; Biemelt, T.; Helmer, A.; Oschatz, M.; Brückner, J.; Althues, H.; Kaskel, S. ZnO Hard Templating for Synthesis of Hierarchical Porous Carbons with Tailored Porosity and High Performance in Lithium-Sulfur Battery. *Adv. Funct. Mater.* **2015**, *25*, 287−297.
(38) Hepp, M.; Wang, H.; Derr, K.; Delacroix, S.; Ronneberger, S.; Loeffler, F. F.; Butz, B.; Strauss, V. Trained Laser-Patterned Carbon as High-Performance Mechanical Sensors. *npj Flexible Electron.* **2022**, *6*, No. 3.
(39) Kossmann, J.; Sánchez-Manjavacas, M. L. O.; Zschiesche, H.; Tarakina, N. V.; Antonietti, M.; Albero, J.; López-Salas, N. Cu II /Cu I Decorated N-Doped Carbonaceous Electrocatalysts for the Oxygen Reduction Reaction. *J. Mater. Chem. A* **2022**, *10*, 6107−6114.
(40) Sadezky, A.; Muckenhuber, H.; Grothe, H.; Niessner, R.; Pöschl, U. Raman Microspectroscopy of Soot and Related Carbonaceous Materials: Spectral Analysis and Structural Information. *Carbon* **2005**, *43*, 1731−1742.
(41) Pawlyta, M.; Rouzaud, J.-N.; Duber, S. Raman Microspectroscopy Characterization of Carbon Blacks: Spectral Analysis and Structural Information. *Carbon* **2015**, *84*, 479−490.
(42) Schuepfer, D. B.; Badaczewski, F.; Guerra-Castro, J. M.; Hofmann, D. M.; Heiliger, C.; Smarsly, B.; Klar, P. J. Assessing the Structural Properties of Graphitic and Non-Graphitic Carbons by Raman Spectroscopy. *Carbon* **2020**, *161*, 359−372.
(43) Bandis, C.; Scudiero, L.; Langford, S. C.; Dickinson, J. T. Photoelectron Emission Studies of Cleaved and Excimer Laser Irradiated Single-Crystal Surfaces of NaNO3 and NaNO2. *Surf. Sci.* **1999**, *442*, 413−419.
(44) Kazansky, L. P.; Pronin, Y. E.; Arkhipushkin, I. A. XPS Study of Adsorption of 2-Mercaptobenzothiazole on a Brass Surface. *Corros. Sci.* **2014**, *89*, 21−29.
(45) Biesinger, M. C.; Lau, L. W. M.; Gerson, A. R.; Smart, R. S. C. Resolving Surface Chemical States in XPS Analysis of First Row Transition Metals, Oxides and Hydroxides: Sc, Ti, V, Cu and Zn. *Appl. Surf. Sci.* **2010**, *257*, 887−898.
(46) Wöll, C. The Chemistry and Physics of Zinc Oxide Surfaces. *Prog. Surf. Sci.* **2007**, *82*, 55−120.
(47) Smith, M.; Scudiero, L.; Espinal, J.; McEwen, J. S.; Garcia-Perez, M. Improving the Deconvolution and Interpretation of XPS Spectra from Chars by Ab Initio Calculations. *Carbon* **2016**, *110*, 155−171.
(48) Wang, H.; Ogolla, C. O.; Panchal, G.; Hepp, M.; Delacroix, S.; Cruz, D.; Kojda, D.; Ciston, J.; Ophus, C.; Knop-Gericke, A.; Habicht, K.; Butz, B.; Strauss, V. Flexible CO2 Sensor Architecture with Selective Nitrogen Functionalities by One-Step Laser-Induced Conversion of Versatile Organic Ink. *Adv. Funct. Mater.* **2022**, No. 2207406.

https://doi.org/10.1021/acsanm.2c04348
ACS Appl. Nano Mater. 2023, 6, 966−975

(49) Lee, M.-G.; Lee, S.-W.; Lee, S.-H. Comparison of Vapor Adsorption Characteristics of Acetone and Toluene Based on Polarity in Activated Carbon Fixed-Bed Reactor. *Korean J. Chem. Eng.* **2006**, *23*, 773−778.
(50) Kwon, S.; Vidic, R.; Borguet, E. The Effect of Surface Chemical Functional Groups on the Adsorption and Desorption of a Polar Molecule, Acetone, from a Model Carbonaceous Surface, Graphite. *Surf. Sci.* **2003**, *522*, 17−26.
(51) Su, C.; Guo, Y.; Yu, L.; Zou, J.; Zeng, Z.; Li, L. Insight into Specific Surface Area, Microporosity and N, P Co-Doping of Porous Carbon Materials in the Acetone Adsorption. *Mater. Chem. Phys.* **2021**, *258*, No. 123930.
(52) Chen, R.; Han, N.; Li, L.; Wang, S.; Ma, X.; Wang, C.; Li, H.; Li, H.; Zeng, L. Fundamental Understanding of Oxygen Content in Activated Carbon on Acetone Adsorption Desorption. *Appl. Surf. Sci.* **2020**, *508*, No. 145211.
(53) Tang, M.; Huang, X.; Peng, Y.; Lu, S. Hierarchical Porous Carbon as a Highly Efficient Adsorbent for Toluene and Benzene. *Fuel* **2020**, *270*, No. 117478.
(54) Lu, S.; Huang, X.; Tang, M.; Peng, Y.; Wang, S.; Makwarimba, C. P. Synthesis of N-Doped Hierarchical Porous Carbon with Excellent Toluene Adsorption Properties and Its Activation Mechanism. *Environ. Pollut.* **2021**, *284*, No. 117113.
(55) Naeem, S.; Baheti, V.; Wiener, J.; Marek, J. Removal of Methylene Blue from Aqueous Media Using Activated Carbon Web. *J. Text. Inst.* **2017**, *108*, 803−811.
(56) Rafatullah, M.; Sulaiman, O.; Hashim, R.; Ahmad, A. Adsorption of Methylene Blue on Low-Cost Adsorbents: A Review. *J. Hazard. Mater.* **2010**, *177*, 70−80.
(57) Hang, P. T. Methylene Blue Absorption by Clay Minerals. Determination of Surface Areas and Cation Exchange Capacities (Clay-Organic Studies XVIII). *Clays Clay Miner.* **1970**, *18*, 203−212.
(58) Lucas, G.; Burdet, P.; Cantoni, M.; Hébert, C. Multivariate Statistical Analysis as a Tool for the Segmentation of 3D Spectral Data. *Micron* **2013**, *52*−*53*, 49−56.

https://doi.org/10.1021/acsanm.2c04348
ACS Appl. Nano Mater. 2023, 6, 966−975